

# Electronically Coupled, Two-Dimensional Assembly of $\text{Cu}_{1.1}\text{S}$ Nanodiscs for Selective Vapor Sensing Applications

Sonam Maiti,<sup>†,‡</sup> Santanu Maiti,<sup>‡</sup> Yvonne Joseph,<sup>§</sup> Andreas Wolf,<sup>||</sup> Wolfgang Brütting,<sup>⊥</sup> Dirk Dorfs,<sup>||</sup> Frank Schreiber,<sup>‡,‡</sup> and Marcus Scheele<sup>\*,†,‡,§</sup>

<sup>†</sup>Institute of Physical and Theoretical Chemistry, University of Tübingen, Auf der Morgenstelle 18, 72076 Tübingen, Germany

<sup>‡</sup>Institute of Applied Physics, University of Tübingen, Auf der Morgenstelle 10, 72076 Tübingen, Germany

<sup>§</sup>Institute of Electronic and Sensor Materials, TU Bergakademie Freiberg, Gustav-Zeuner-Straße 3, 09599 Freiberg, Germany

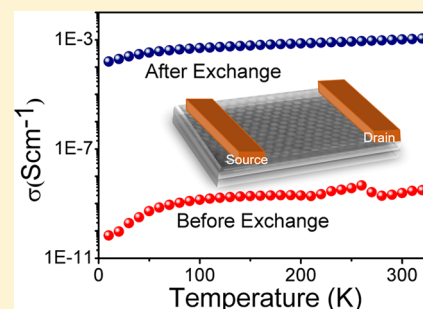
<sup>||</sup>Institute of Physical Chemistry and Electrochemistry, Leibniz Universität Hannover, Callinstr. 3A, 30167 Hannover, Germany

<sup>⊥</sup>Institute of Physics, University of Augsburg, Universitätsstrasse 1, 86159 Augsburg, Germany

<sup>#</sup>Center for Light-Matter Interaction, Sensors & Analytics LISA+, University of Tübingen, Auf der Morgenstelle 15, 72076 Tübingen, Germany

## Supporting Information

**ABSTRACT:** We study temperature-dependent charge transport in two-dimensional assemblies of copper sulfide nanodiscs in the covellite crystal phase ( $\text{Cu}_{1.1}\text{S}$ ). To enhance interparticle coupling, we cross-link the nanocrystals with the organic  $\pi$ -system Cu-4,4',4'',4'''-tetraaminophthalocyanine and observe an increase in the conductivity by 6 orders of magnitude. The electrical properties of monolayers of this hybrid ensemble are consistent with a two-dimensional semiconductor and exhibit two abrupt changes at discrete temperatures (120 and 210 K), which may be interpreted as phase changes. X-ray scattering experiments serve to study the importance of electronic conjugation in the organic  $\pi$ -system vs interparticle spacing for efficient charge transport. Applying the hybrid ensemble as a chemiresistor in organic vapor sensing experiments reveals a strong selectivity between polar and nonpolar analytes, which we discuss in light of the role of the organic  $\pi$ -system and its metal center.



## INTRODUCTION

Two dimensional (2D) semiconductor materials (such as  $\text{WS}_2$ ) have great potential for application in photodiodes, solar cells, photocatalysis, batteries, and thermoelectric and light-emitting diodes.<sup>1–5</sup> While the charge carrier mobility in single-crystalline grains may exceed that of crystalline silicon, it is challenging to synthesize these materials with macroscopic lateral domain sizes.<sup>5</sup> In contrast, granular ensembles of 2D conductors can be obtained in large quantities and assembled into macroscopic thin films, however with significantly lower mobilities.<sup>6</sup> Charge carrier transport in such granular 2D materials occurs typically via hopping, which was first described by Mott with the concept of variable-range hopping (VRH), assuming that carriers hop between localized states over a characteristic, temperature-dependent hopping distance.<sup>7,8</sup> While the density of states (DOS) is considered to be constant in this model, the electrical conductivity varies with temperature as  $\sigma(T) = \sigma_0 \exp[-(T_{\text{Mott}}/T)^x]$ . Here,  $T$  is the absolute temperature,  $\sigma_0$  the attempt frequency for a hopping event,  $T_{\text{Mott}}$  the characteristic Mott temperature, and  $n = 1/(D + 1)$ , where  $D$  is the dimensionality of the conductor. Thus, for a 2D material,  $\ln \sigma$  is proportional to  $T^{-1/3}$ . Efros and Shklovskii later pointed out that for sufficiently low temperatures, the DOS near the Fermi level ( $E_F$ ) is not constant and

Coulomb interactions give rise to a soft gap in the density of states. In this regard, it has been demonstrated that the DOS near  $E_F$  vanishes linearly with energy for a 2D system.<sup>9–11</sup> This has been explained with the electron–hole Coulomb interaction to be overcome when an electron hops from one site to another.<sup>12</sup> For this ES VRH mechanism, the conductivity varies with temperature as  $\sigma(T) = \sigma_0 \exp[-(T_{\text{ES}}/T)^{1/2}]$ . Here,  $\ln \sigma$  is always proportional to  $T^{-1/2}$  regardless of the dimensionality of the system, which merely affects the characteristic temperature  $T_{\text{ES}}$ .<sup>13</sup> Therefore, for a granular 2D semiconductor, one can expect  $\ln \sigma \sim T^{-1/2}$  for sufficiently low temperatures and  $\ln \sigma \sim T^{-1/3}$  for higher temperatures.

In this work, we use this characteristic behavior to examine under which conditions ensembles of covellite nanocrystals ( $\text{Cu}_{1.1}\text{S}$  NCs) behave collectively like a 2D semiconductor. We chose  $\text{Cu}_{1.1}\text{S}$  due to its low toxicity and rich redox chemistry, which renders it attractive for environmentally benign applications in optoelectronics and sensing.<sup>14–16</sup> Previous attempts to tune the transport properties of copper sulfide NC

Received: June 1, 2018

Revised: August 18, 2018

Published: September 24, 2018



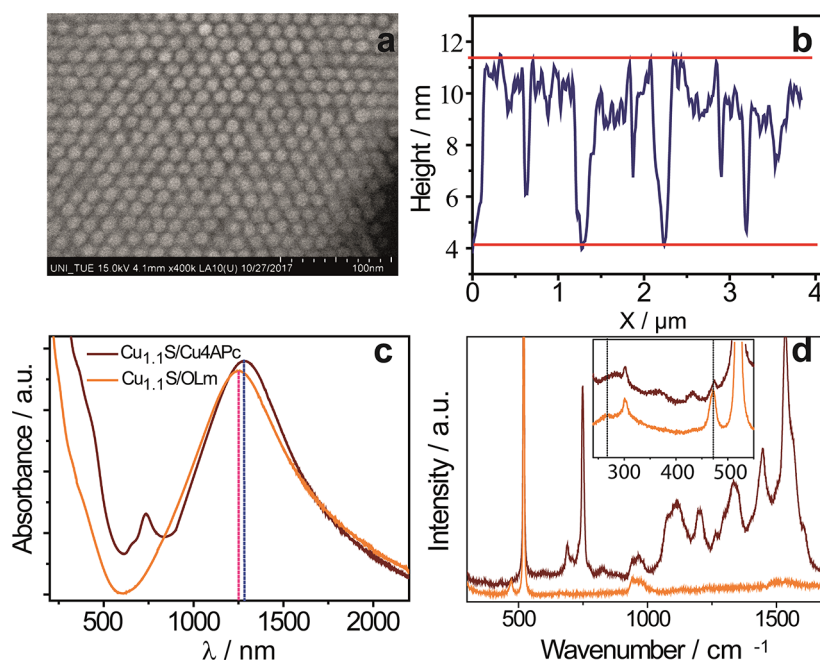


**Figure 1.** (a) SEM image and (b) height profile of a typical  $\text{Cu}_{1.1}\text{S}/\text{Cu4APc}$  film determined by atomic force microscopy (see Figure S3b for the original image). (c) UV-vis-NIR absorption spectra of as-prepared  $\text{Cu}_{1.1}\text{S}$  superlattice before and after ligand exchange (orange and dark red curves, respectively). (d) Raman spectra of as-prepared  $\text{Cu}_{1.1}\text{S}$  nanocrystal thin films before and after ligand exchange (same color code as in part c). The inset highlights the spectral regime around the S–S stretching bands.

ensembles employed thermal doping, electrophoretic deposition and/or ligand exchange with small molecules, such as 1,2-ethanedithiol (EDT), hydrazine, mercaptopropionic acid, or ethylenediamine.<sup>17–21</sup> Depending on the surface modification, Copper sulfide NC ensembles have displayed 3D VRH transport, Arrhenius-type, nearest neighbor hopping or non-monotonic temperature dependencies.<sup>18,19</sup> Typical conductivities ranged between  $10^{-4}$ ,  $10^{-2}$ , and  $75 \text{ S cm}^{-1}$  for EDT-functionalization, treatment with hydrazine, and electrophoretic deposition, respectively. Here, we take a different approach toward increasing electronic coupling in  $\text{Cu}_{1.1}\text{S}$  NC films by functionalizing their surface with the relatively large (1.2 nm), but fully conjugated molecule Cu-4,4',4'',4'''-tetraaminophthalocyanine (Cu4APc) similar to other types of coupled organic–inorganic nanostructures.<sup>22</sup> We discuss the transport behavior of this hybrid material in the context of potential 2D Mott VRH and demonstrate its perspectives for solvent vapor sensing.

## 2. METHODS

**2.1. Synthesis of  $\text{Cu}_{1.1}\text{S}$  Nanocrystals.**  $\text{Cu}_{1.1}\text{S}$  NCs were prepared by adapting the heat-up synthesis procedure from Xie et al.<sup>23</sup>

**2.2. Synthesis of Ligands.** Copper 4,4',4'',4'''-tetraaminophthalocyanine (Cu4APc) was synthesized following a previously reported procedure.<sup>24</sup> For the structural formula, see Figure S1.

**2.3. Thin-Film Preparation and Ligand Exchange.** In this work, electronically coupled, ordered NC superlattice films were assembled at the liquid/air interface.<sup>25,26</sup> Initially, the native oleylamine passivated, disc-shaped  $\text{Cu}_{1.1}\text{S}$  NCs (diameter of  $12.7 \pm 1.7 \text{ nm}$ , and a thickness of  $5.8 \pm 0.7 \text{ nm}$ ) film was prepared by controlling the evaporation of toluene solvent in DMSO solution in a home-built Teflon chamber. A reference sample was prepared by transferring this film on to

a Si-substrate. For Cu4APc cross-linked NCs, a solution of Cu4APc in DMSO was slowly injected into the subphase by a syringe in order to ligand-exchange the assembled NC film floating above the DMSO phase. Finally, the free-floating ligand-exchanged NC superlattice was transferred to substrates by retracting the solution from the bottom of the chamber (Figure S2).

**2.4. Instrumentation.** Scanning transmission electron microscopy (STEM, Hitachi SU 8030 microscope operating at 30 kV) was employed to determine the particle size and shape. Optical measurements were performed on solid state films on glass substrates using an UV-vis-NIR spectrometer (Agilent Technologies, Cary 5000). Grazing-incidence small-angle X-ray scattering (GISAXS)<sup>27</sup> was carried out with a laboratory instrument (Xeuss 2.0, Xenocs, France) using  $\text{Cu K}\alpha$  radiation ( $\lambda = 1.5418 \text{ \AA}$ ). The samples were probed with a focused X-ray beam of size  $0.5 \times 0.5 \text{ mm}^2$  at incidence angle of  $0.22^\circ$ . The GISAXS images were collected with a 2D Pilatus 300 K, having  $487 \times 619$  pixels. The detector was placed at a distance of 2496 mm, determined using Ag-behenate as reference sample. X-ray reflectivity (XRR) data from the sample was collected in specular geometry with a laboratory source ( $\text{Cu K}\alpha$ ; GE Inspection Technologies, Germany). The surface morphology was measured by AFM using a JPK Nanowizard II instrument in tapping mode under ambient conditions. Image analysis was performed with Gwyddion. Raman spectra were acquired using a Horiba Jobin Yvon Labram HR 800 spectrometer with a CCD-1024  $\times$  256-OPEN-3S9 detector. Excitation for Raman was performed using a He:Ne laser (wavelength 633 nm). Electrical measurements were performed in a glovebox at room temperature with a homemade probe station using a Keithley 2634B dual source-meter unit, controlled by the included test script builder program. The NC films after ligand exchange were deposited on commercially available bottom-gate,

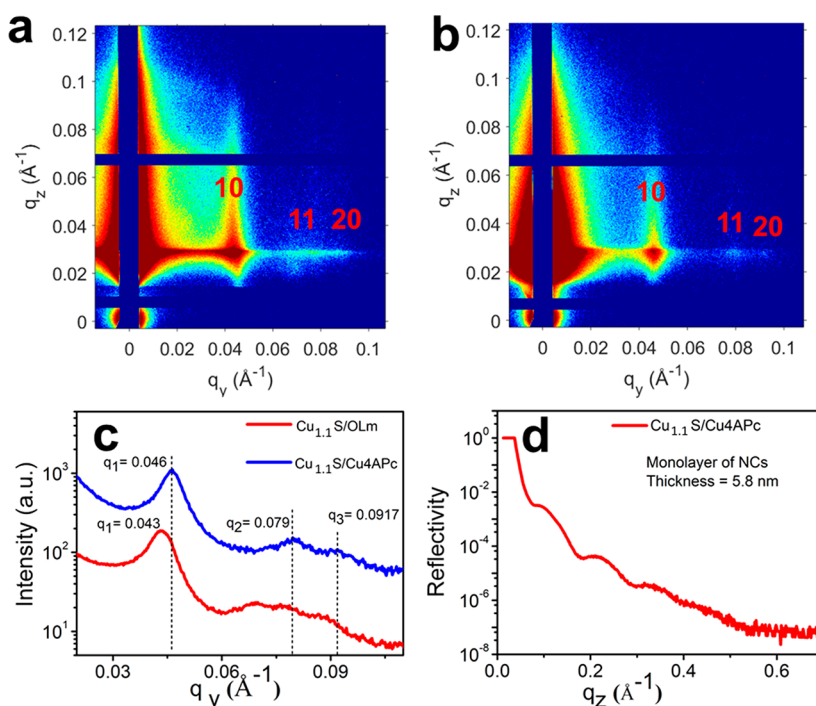


**Figure 2.** (a) GISAXS patterns of self-assembled  $\text{Cu}_{1.1}\text{S}$  NCs coated with OA. (b) GISAXS pattern of Cu4APc ligand induced assembly  $\text{Cu}_{1.1}\text{S}$  NCs. Both patterns show long-range highly ordered 2D hexagonal superlattices. (c) Extracted line profiles from the corresponding GISAXS images along in-plane wave vector  $q_y$ . To improve the statistics of the line profiles the signals were integrated along the  $q_z$  direction. (d) X-ray reflectivity profile of  $\text{Cu}_{1.1}\text{S}/\text{Cu4APc}$  film.

bottom-contact transistor substrates (Fraunhofer Institute for Photonic Microsystems, Dresden, Germany) with interdigitated Au electrodes of 10 nm width and 2.5  $\mu\text{m}$  channel length followed by annealing at 250  $^\circ\text{C}$  for 2 h under nitrogen atmosphere. The temperature-dependent charge transport properties of the NC thin-films were measured by a Lake-Shore CRX-6.5K probe station, equipped with a Keithley 2636B dual source-meter unit and a Lake Shore temperature controller (model 336). For investigating the vapor sensing properties, the NC films were deposited on commercially available glass substrates with interdigitated gold electrode structure (90 finger pairs, 10  $\mu\text{m}$  microelectrode gap and a circular area with a diameter of 3.5 mm; “ED-IDE1-Au” by micrux Technologies). The sensitivity of the films was characterized by dosing them with vapors of 4-methyl-2-pentanone (4M2P), toluene, 2-propanol, and water while monitoring their resistances at 0.1 V. All vapor sensing experiments were carried out at room temperature (ca. 25  $^\circ\text{C}$ ) at a flow rate of 400  $\text{mL min}^{-1}$ . As all vapors have comparable vapor pressures (21, 29, 20, and 23 mbar at 20  $^\circ\text{C}$ , respectively),<sup>28</sup> differences in the response of the samples are expected to arise mainly from their chemical nature (polarity and structural features) and not from the differences in vapor pressure.

### 3. RESULTS

Figure 1a depicts a typical SEM image of Cu4APc cross-linked  $\text{Cu}_{1.1}\text{S}$  NCs assembled into a hexagonal superlattice. The disk-shaped NCs have an average diameter of  $12.7 \pm 1.7$  nm and a thickness of  $5.8 \pm 0.7$  nm as determined from high resolution scanning electron micrographs (Figure S3a). Height profiles obtained by atomic force microscopy (AFM, Figure 1b and Figure S3b) show that the average superlattice thickness is one

monolayer (6 nm). Figure 1c displays the UV–vis–NIR spectra of the as-prepared  $\text{Cu}_{1.1}\text{S}$  NCs before (orange) and after ligand exchange with Cu4APc (dark red) on quartz substrates. The strong NIR absorption with a maximum around 1250 nm is characteristic for a localized surface plasmon resonance (LSPR) due to copper vacancies.<sup>29–31</sup> In addition, the ligand exchanged film displays a new peak at 736 nm corresponding to the appearance of the singlet absorption of Cu4APc.<sup>13</sup> Raman spectroscopy provides further evidence for a successful ligand exchange (Figure 1d). While the vibrational spectrum of the as-prepared  $\text{Cu}_{1.1}\text{S}$  NCs before ligand exchange (orange curve) features mainly a weak band at 265  $\text{cm}^{-1}$  (see inset) and a sharp band at 471  $\text{cm}^{-1}$  due to S–S stretching vibrations, additional bands at 747, 1115, 1345, 1447, 1535, and 1605  $\text{cm}^{-1}$  appear after ligand exchange with Cu4APc.<sup>32,33</sup> (Note: The bands observed near 521 and 966  $\text{cm}^{-1}$  correspond to the optical phonon modes of the Si substrate.) Furthermore, the S–S stretching bands shift to 267 and 474  $\text{cm}^{-1}$  (see inset), which is often attributed to a binding interaction with the surface of the particles. These Raman spectra for both films are in good agreement with the existing literature on crystalline  $\text{Cu}_{1.1}\text{S}$  NCs.<sup>33,34</sup>

The structural changes of the  $\text{Cu}_{1.1}\text{S}$  NC superlattice before and after ligand exchange are determined by GISAXS on Si-substrates in Figure 2, parts a and b. The appearance of several intense scattering truncation rods, extended along the  $q_z$ -direction at different  $q_y$ -positions corresponds to a long-range ordered monolayer superlattice formation for both cases. The ratio of the relative peak positions is 1:  $\sqrt{3}$ :2—which is a characteristic of two-dimensional hexagonal superlattices for both cases and can be indexed with 10, 11, and 20 superlattice planes.<sup>35</sup> The significant changes of the correlation peak positions along the  $q_y$ -direction for both samples are

additionally displayed with line profiles (Figure 2c). The lattice constants, which equal the nearest-neighbor distance in hexagonal lattices, are  $16.8 \pm 0.1$  and  $15.7 \pm 0.1$  nm before and after ligand exchange, respectively. We attribute the decrease of 1.1 nm to the effect of replacing the larger oleic acid ligand ( $\sim 2$  nm) by the more compact Cu4APc ( $\sim 1.2$  nm) molecule. The XRR profile in Figure 2d features multiple Kiessig oscillations, from which we determine the thickness of the NC film on the substrate to 5.8 nm, in good agreement with our AFM data.<sup>36</sup>

For charge transport studies, the  $\text{Cu}_{1.1}\text{S}$  NC films were deposited on Si-substrates with prepatterned gold contacts. Since the  $I/V$  characteristics were slightly field-dependent, all conductivities were measured in the low-field regime by fitting the linear current response to a voltage sweep from  $-200$  to  $+200$  mV (see Figures S4 and S5). We find an enhancement by 6 orders of magnitude after ligand exchange with Cu4APc in the electrical conductivity of the NC superlattice, providing clear evidence for the improved coupling. To determine the transport mechanism in the 2D superlattices of NCs before and after ligand exchange, we perform temperature-dependent conductivity measurement from 30 to 300 K in Figure 3a. In both cases,  $\sigma$  of the film increases with increasing temperature, which is the typical behavior of a semiconductor. However, as evident for the unexchanged sample and—to a lesser degree—for the Cu4APc-functionalized NCs as well (inset in Figure 3a),  $\sigma(T)$  deviated from a simple monotonic increase, implying that the charge transport cannot be described by a single hopping model. While the origin of this anomaly is not clear, it has been observed before for arrays of  $\text{Cu}_{1.1}\text{S}$  and tends to be more pronounced for less coupled NCs.<sup>19,37</sup> The deviation from a single hopping model is further evidenced for the Cu4APc-capped  $\text{Cu}_{1.1}\text{S}$  films in Figure 3b, where we plot the  $\sigma(T)$  data according to  $\ln \sigma = \ln \sigma_0 - \left(\frac{T_0}{T}\right)^{1/x}$  with  $x = 1, 2, 3$ ,

or 4. Evidently, none of the common temperature coefficients results in a satisfactory fit over the entire temperature range. To exemplify this, we display linear fits to the data as dashed lines. For  $x = 2, 3$ , and 4, this satisfactorily describes the data at low temperatures (30–120 K), but increasingly deviates from a simple linear relationship (in this mode of plotting the data) above this range. For  $x = 1$ , no linear relationship over a reasonably large temperature window could be established.

Another way of testing a certain transport mechanism is to plot the derivative  $d(\log \sigma)/d(\log T)$  against  $\log T$  as illustrated in Figure 3c<sup>38</sup> and determining  $x$  from the slope,  $m$ , of a linear fit to the data as  $x = -1/m$ . The unusual, nonmonotonic  $\sigma(T)$  behavior is readily visible in this plot with three distinct temperature regimes, namely 30–120 K, 120–210 K and 210–300 K, which are separated by abrupt changes in the derivative  $d(\log \sigma)/d(\log T)$ . We note several previous reports about presumed phase transitions in copper sulfide at low temperatures, which we tentatively hold responsible for our observation.<sup>19,37,39</sup> Between 30 and 120 K, we find  $x = 2.1$  and a reasonable R-squared confidence of 90%, suggesting a VRH ES transport mechanism in this temperature window. For 120–210 K, the slope notably flattens and we derive  $x = 3.0$  in excellent agreement with Mott 2D VRH. However, an  $R^2$  confidence of only 53% cannot entirely rule out the possibility of Mott 3D VRH due to the small differences between the two mechanisms in the expected slope. Above 210 K, the  $R^2$  confidence decreases to 18%, and a meaningful fit becomes

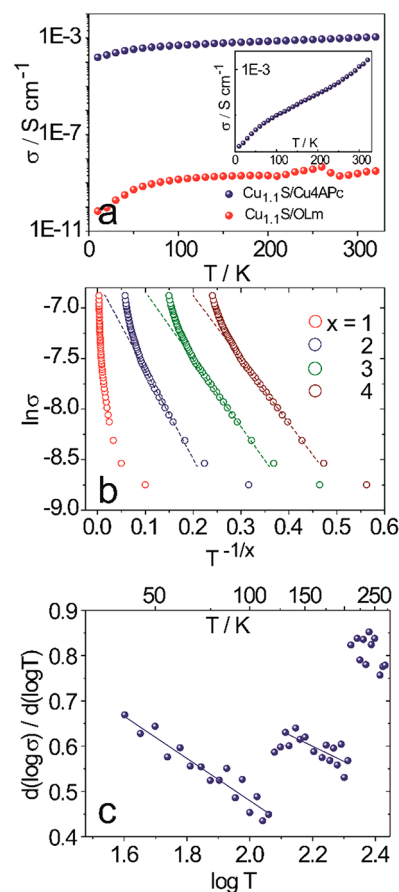


**Figure 3.** (a) Temperature-dependent electrical conductivity measurement of  $\text{Cu}_{1.1}\text{S}$  nanocrystal films from 30 to 320 K. Red circles: OLm-capped  $\text{Cu}_{1.1}\text{S}$  NC films and blue circles:  $\text{Cu}_{1.1}\text{S}$  NC films cross-linked with Cu4APc. Inset: linear plot of the Cu4APc-capped  $\text{Cu}_{1.1}\text{S}$  film for better visualization. (b)  $\ln \sigma$  vs  $T^{-1/x}$  for  $x = 1-4$  as assigned by the color legend for  $\text{Cu}_{1.1}\text{S}$  NC films cross-linked with Cu4APc. Dashed lines are linear fits for a fixed temperature window of 30–120 K. (c) Derivative  $d(\log \sigma)/d(\log T)$  vs  $\log T$  for the same data set as in part b. Solid lines are linear fits for fixed temperature windows of 30–120 and 120–210 K, respectively.

impossible. We suspect that this may be due to the already mentioned anomaly in this temperature range (see Figure 3a).

In addition to studying the transport characteristics of  $\text{Cu}_{1.1}\text{S}/\text{Cu4APc}$  monolayers, we seek to take advantage of the high active surface area of the material for vapor sensing. The basic idea is that adsorption of vaporized molecules on and into the  $\text{Cu}_{1.1}\text{S}/\text{Cu4APc}$  monolayer may induce a change in resistance, which serves as feedback for sensing. Figure 4a presents the typical resistance change ( $\Delta R/R_0$ ) at room temperature upon exposure to 4M2P vapor with concentrations in the range of 100–5000 ppm (three exposure cycles of 120 s each). We observe a fast (few seconds) and fully reversible, approximately rectangular response, which increases with increasing analyte concentration at the same operating temperature and 0% relative humidity. Four types of vapor analytes are used in this study, i.e. 4M2P, toluene, 1-propanol, and water to check the chemical selectivity. Figure 4b compares the response of the NC film to these four analytes after exposure to 5000 ppm. While toluene vapor exhibits a significant but slightly weaker response compared to 4M2P vapor, the two polar analytes 1-propanol and water invoke almost no response.

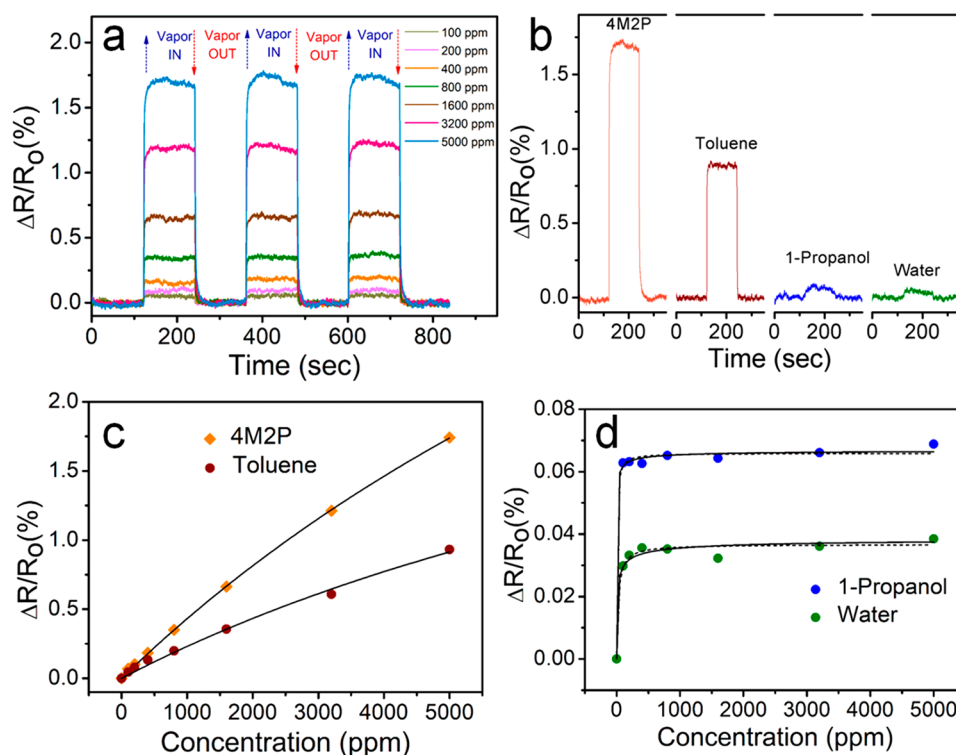


**Figure 4.** (a) Transient vapor response traces of  $\text{Cu}_{1.1}\text{S}/\text{Cu4APc}$  film toward 100 to 5000 ppm of 4M2P at 0% relative humidity. (b) Responses of the  $\text{Cu}_{1.1}\text{S}/\text{Cu4APc}$  films to exposure with 5000 ppm 4M2P vapor, toluene vapor, water vapor, and 1-propanol vapor. (c) Response amplitudes plotted versus the gas-phase concentration of 4M2P and toluene. (d) Response amplitudes plotted versus the gas-phase concentration of 1-propanol and water. The solid lines are the Langmuir fits according to a 1st order adsorption model (i.e., eq 1) and the dashed lines are the Langmuir fits according to a 2nd order adsorption model (i.e., eq 2).

We gain further insight into the sensor response and analyte/film interactions by fitting the concentration-dependent change in resistance for all four analytes with a Langmuir adsorption using the equation

$$\frac{\Delta R}{R_0} = \left[ \frac{\Delta R}{R_0} \right]_s \frac{K_b C_{\text{vapor}}}{1 + K_b C_{\text{vapor}}} \quad (1)$$

where  $[\Delta R/R_0]_s$  and  $K_b$  are the relative change of resistance at saturation and the binding constant, respectively, and  $C_{\text{vapor}}$  is the concentration of the analyte in the gas phase.<sup>28</sup>

We find that the first order Langmuir adsorption model in eq 1 reflects well the behavior for 4M2P and toluene as displayed in Figure 4c. In contrast, no satisfactory fits could be obtained in this way for the analytes 1-propanol and water, which is why we applied a second order Langmuir adsorption model according to eq 2, which described the experimental data more adequately (Figure 4d).

$$\frac{\Delta R}{R_0} = \left[ \frac{\Delta R}{R_0} \right]_s \frac{K_b \sqrt{C_{\text{vapor}}}}{1 + K_b \sqrt{C_{\text{vapor}}}} \quad (2)$$

The fitting parameters, such as the relative differential resistance responses at saturation  $[\Delta R/R_0]_s$  and the binding constants  $K_b$  obtained from the first and second order Langmuir adsorption model for all four analytes at room temperature are given in Table 1.

#### 4. DISCUSSION

In addition to providing evidence for the chemical modifications, the spectroscopic data in Figure 1 also

**Table 1. Experimental Sensor Responses, i.e., Relative Changes of Resistance at Saturation  $[\Delta R/R_0]_s$  and Binding Constants  $K_b$ , Obtained from the Langmuir Fits for  $\text{Cu}_{1.1}\text{S}/\text{Cu4APc}$  Thin Films at Room Temperature**

NC film	analyte	$[\Delta R/R_0]_s$ (%)	$K_b$
$\text{Cu}_{1.1}\text{S}/\text{Cu4APc}$	4M2P	7.13	$6.43602 \times 10^{-5} \text{ (M}^{-1}\text{)}$
	toluene	3.51	$7.03732 \times 10^{-5} \text{ (M}^{-1}\text{)}$
	1-propanol	0.067	$1.11619 \text{ (M}^{-0.5}\text{)}$
	water	0.039	$0.29583 \text{ (M}^{-0.5}\text{)}$

highlights the structural changes occurring in the NC ensemble during surface functionalization with Cu4APc. We attribute the 34 nm red-shift of the LSPR transition to a reduced interparticle distance due to the shorter length of Cu4APc (12 Å) compared to oleylamine (20 Å). As the interparticle spacing narrows, dipole–dipole interactions between the NCs strengthen, which is known to cause a red-shift in the LSPR band.<sup>40</sup> In addition, alterations in the dielectric environment of the NCs by the new surface chemistry can also affect the position of the LSPR. The anticipated contraction of the interparticle spacing is quantified by the GISAXS data in Figure 2 to a net decrease of 11 Å. It is noteworthy that even after this contraction, the average interparticle spacing is  $30 \pm 17$  Å and, thus, the NCs remain spatially well separated. In this light, the room-temperature conductivity of  $1 \text{ mS cm}^{-1}$  is quite remarkable (Figure 3a) and even higher than that of EDT treated  $\text{Cu}_{1.1}\text{S}$  NCs, despite the much shorter length of the molecular linker (4 Å).<sup>20</sup> In addition, the conductivity increase by 6 orders of magnitude following the interparticle contraction during ligand exchange highlights the sensitivity

of the material toward further structural changes, such as those induced by swelling upon exposure to a solvent vapor. To test this idea, we chose the four vapor analytes investigated in Figure 4, which differ significantly in their chemical affinity and permittivity (toluene, 2.4 (hydrophobic); 4M2P, 13.11 (hydrophilic); 1-propanol, 20.8 (H-bonding); and water, 80.1 (polar H-bonding)).<sup>41</sup> As detailed in Table 1, the Cu4APc-capped Cu<sub>1.1</sub>S NC monolayers are significantly more sensitive toward analytes of low permittivity (4M2P and toluene), while the two polar analytes 1-propanol and water bind more strongly to the film as indicated by the larger binding constants  $K_b$  (Table 1) as well as the strong curvature of the response (Figure 4d).<sup>42</sup>

We consider several possible reasons for the different behavior of 4M2P/toluene vs 1-propanol/water: (1) Water and 1-propanol are quite small and compact molecules, such that swelling effects exerted by these species are expected to be relatively small. (2) As shown in previous findings by Olichwer et al. on hydrophobic superlattices of dodecanethiol (DDT)-stabilized Au NCs, 1-propanol adsorbs predominantly on the surface of the film with little contribution to film swelling.<sup>43</sup> However, Cu4APc is significantly less hydrophobic than DDT, such that this reasoning may not fully apply here. (3) The metal center of tetraaminophthalocyanines possess a high affinity toward 1-propanol and water.<sup>44</sup> With just one metal per molecule, we expect this particular binding site to saturate quickly, even at low dosing concentrations. As a very crude estimate, one may expect 3 molecules per nm<sup>2</sup> on the surface of each nanocrystal,<sup>45</sup> corresponding to 300 metal center binding sites as an upper limit. Considering the active area of the interdigitated electrodes of the transducer (38.5 mm<sup>2</sup>) and assuming a monolayer coverage with Cu<sub>1.1</sub>S particles (diameter: 12.7 nm) with hexagonal packing (74% fill fraction) yields  $5.6 \times 10^{10}$  particles, corresponding to  $1.7 \times 10^{13}$  metal center binding sites in the entire active area. At room temperature, there are roughly  $2.5 \times 10^{22}$  gas molecules/L, and, thus,  $2.5 \times 10^{18}$  1-propanol/water molecules per liter at a dosing concentration of 100 ppm. At a flux of 400 mL/min, saturation is expected instantaneously for this scenario after roughly 1 ms of exposure time in agreement with our observations (see Figure 4, parts b and d). Such a small density of binding sites could possibly enable very low limits of detection as indicated by Figure 4d, provided a sufficient signal-to-noise ratio exists.

In contrast, for the nonpolar analytes toluene and 4M2P, a strong affinity to the phthalocyanine metal center does not exist such that they are weakly adsorbed within the nonpolar ligand matrix and invoke swelling of the NC film. This induced expansion of the interparticle spacing is expected to significantly increase the resistance (as demonstrated in Figure 3a), which appears to be the major sensing mechanism for this material, explaining the selectivity for the two analytes toluene and 4M2P.<sup>8,28</sup> The magnitude of the relative response should be viewed in the context of the very thin layer thickness of  $\leq 10$  nm, a fast recovery of the sensors within a second time regime and a nearly rectangular sensor response. Thicker films may exhibit a stronger, but slower sensing response. In comparison with other previously reported chemiresistors based on NC ensembles for room temperature vapor sensing, these preliminary sensing measurements are encouraging. For instance, networks of Au NCs cross-linked with a variety of alkanethiols have shown  $\Delta R/R_0$ -values between 0.1 and 10% but suffer from gradual degradation in air due to oxidation of

the thiol cross-linkers.<sup>28,42,46–48</sup> Utilizing more durable tin-doped indium oxide NCs yielded  $\Delta R/R_0$ -values of 2–3%.<sup>49,50</sup> Higher values of 80–500% are typically only obtained for very large analyte concentrations or at elevated temperatures (300 °C).<sup>51,52</sup> For example, ZnO nanoflowers decorated with Au NCs have been reported to exhibit a  $\Delta R/R_0$  of 7500% toward 100 ppm acetone, however only at a working temperature of 270 °C.<sup>53</sup> The material investigated in the present paper is operative under ambient conditions, unoptimized and holds the potential for selective vapor sensing at low detection limits due to its heterostructure as outlined above.

The temperature-dependent transport data of Cu4APc-capped Cu<sub>1.1</sub>S NC monolayers in Figure 3 are consistent with the picture of a two-dimensional conductor. At low temperatures ( $30 < T < 120$  K), the transport mechanism is satisfactorily described with ES VRH, supposedly because of the dominant effect of Coulomb interactions and the opening of a soft gap in the density of states. At higher temperatures, this Coulomb gap closes and the transport data is more adequately described with Mott VRH as indicated by the slope of 0.33 for  $d(\log \sigma)/d(\log T)$  vs  $\log T$  (Figure 3c). As detailed in the Introduction, this is the expected behavior for a granular 2D conductor.

We note that the transport properties of Cu4APc-capped Cu<sub>1.1</sub>S NC films are different from those detailed by Bekenstein et al. for the same type of NCs but different surface ligands, such as thiols of different chain lengths or mercaptopropionic acid, who exclusively found Arrhenius-type NNH over the whole temperature range.<sup>19</sup> In view of the quasi-two-dimensional structure of the films and the relatively large conductivity provided by the conjugated Cu4APc cross-linkers, we suspect that this altered transport behavior may be due to a combination of the unique geometry of the material as well as enhanced coupling between the NCs. This and the large interparticle spacing ( $30 \pm 17$  Å) are ideal for resistance-mediated sensing applications of vapors, operating with adsorption and swelling effects, which we have demonstrated with the vapor sensing measurements in Figure 4. Comparative electric transport measurements using thicker films (5–10 monolayers) yield 2–3 orders of magnitude smaller electric conductivities, which we attribute predominantly to large structural inhomogeneities as well as a potentially incomplete ligand exchange (Figure S6).

## 5. CONCLUSION

We assemble Cu<sub>1.1</sub>S NCs capped with the organic  $\pi$ -system Cu4APc at the air–liquid interface into a quasi-2D thin film with significant long-range order and electronic coupling. The coupling is evidenced by a 6 orders of magnitude enhancement in the conductivity as a result of the ligand exchange. Temperature-dependent electrical transport measurements are discussed in the context of two-dimensional variable range hopping, the effect of the quasi-2D structure, and the presence of the conjugated linker. Resistivity-based vapor sensing measurements reveal a selective sensitivity for nonpolar analytes, which is facilitated by a large interparticle spacing of  $30 \pm 17$  Å. The results of this study show how combining organic  $\pi$ -systems and copper-deficient covellite NCs rewards electrically conductive, quasi-2D films, which are solution-processable and attractive for vapor sensing applications.

## ■ ASSOCIATED CONTENT

### Supporting Information

The Supporting Information is available free of charge on the ACS Publications website at DOI: 10.1021/acs.jpcc.8b05276.

Structural formula of Cu4APc, schematics of the ligand exchange procedure at the liquid/air interface, high magnification STEM and AFM image of the Cu<sub>1.1</sub>S NC film, current–voltage (*I*–*V*) curves before and after ligand exchange and the evaluation of contact resistance applying transmission line method (TLM), field-dependence of the *I/V* characteristics, and transport characteristics of thicker films (PDF)

## ■ AUTHOR INFORMATION

### Corresponding Author

\*(M.S.) E-mail: [marcus.scheele@uni-tuebingen.de](mailto:marcus.scheele@uni-tuebingen.de).

### ORCID

Yvonne Joseph: 0000-0003-0697-9646

Dirk Dorfs: 0000-0001-6175-4891

Marcus Scheele: 0000-0002-2704-3591

### Author Contributions

The manuscript was written through contributions of all authors. All authors have given approval to the final version of the manuscript.

### Notes

The authors declare no competing financial interest.

## ■ ACKNOWLEDGMENTS

The authors acknowledge the DFG for support under Grants SCHE1905/3, SCHE1905/4, BR1728/18, and SCHR700/25. We also thank Mrs. Elke Nadler, Institute of Physical and Theoretical Chemistry, University of Tübingen, for performing SEM/STEM measurements using a Hitachi SU 8030 SEM which was partially funded by the DFG under Contract INST 37/829-1 FUGG. Mahdi Samadi Khoshkhoo is gratefully acknowledged for help with vapor sensing measurements.

## ■ REFERENCES

- (1) Huang, X.; Tan, C.; Yin, Z.; Zhang, H. 25th Anniversary Article: Hybrid Nanostructures Based on Two-Dimensional Nanomaterials. *Adv. Mater.* **2014**, *26*, 2185–2203.
- (2) Nasilowski, M.; Mahler, B.; Lhuillier, E.; Ithurria, S.; Dubertret, B. Two-Dimensional Colloidal Nanocrystals. *Chem. Rev.* **2016**, *116*, 10934–10982.
- (3) Maiti, S.; Sanyal, M. K.; Varghese, N.; Satpati, B.; Dasgupta, D.; Dailant, J.; Carriere, D.; Konovolov, O.; Rao, C. N. R. Formation of Single-Crystalline CuS at the Organic-Aqueous Interface. *J. Phys.: Condens. Matter* **2013**, *25*, 395401.
- (4) Zhao, Y.; Burda, C. Development of Plasmonic Semiconductor Nanomaterials with Copper Chalcogenides for a Future with Sustainable Energy Materials. *Energy Environ. Sci.* **2012**, *5*, 5564–5576.
- (5) Wang, Q. H.; Kalantar-Zadeh, K.; Kis, A.; Coleman, J. N.; Strano, M. S. Electronics and Optoelectronics of Two-Dimensional Transition Metal Dichalcogenides. *Nat. Nanotechnol.* **2012**, *7*, 699–712.
- (6) Kelly, A. G.; Hallam, T.; Backes, C.; Harvey, A.; Esmaily, A. S.; Godwin, I.; Coelho, J.; Nicolosi, V.; Lauth, J.; Kulkarni, A.; Kinge, S.; Siebbeles, L. D. A.; Duesberg, G. S.; Coleman, J. N. All-Printed Thin-Film Transistors from Networks of Liquid-Exfoliated Nanosheets. *Science* **2017**, *356*, 69–73.
- (7) Mott, N. F. Conduction in Non-Crystalline Systems. *Philos. Mag.* **1968**, *17*, 1259–1268.
- (8) Aggarwal, M.; Khan, S.; Husain, M.; Ming, T. C.; Tsai, M. Y.; Perng, T. P.; Khan, Z. H. Variable-Range Hopping in Fe<sub>70</sub>Pt<sub>30</sub> Catalyzed Multi-Walled Carbon Nanotubes Film. *Eur. Phys. J. B* **2007**, *60*, 319–324.
- (9) Shklovskii, B. I.; Efros, A. L. *Electronic Properties of Doped Semiconductors*; Springer: Berlin, 1984.
- (10) Efros, A. L.; Shklovskii, B. I. Coulomb Gap and Low Temperature Conductivity of Disordered Systems. *J. Phys. C: Solid State Phys.* **1975**, *8*, L49–L51.
- (11) Khondaker, S.; Shlimak, I.; Nicholls, J.; Pepper, M.; Ritchie, D. Two-Dimensional Hopping Conductivity in a  $\delta$ -Doped GaAs/Al<sub>x</sub>Ga<sub>1-x</sub>As Heterostructure. *Phys. Rev. B: Condens. Matter Mater. Phys.* **1999**, *59*, 4580–4583.
- (12) Joung, D.; Khondaker, S. I. Efros-Shklovskii Variable-Range Hopping in Reduced Graphene Oxide Sheets of Varying Carbon Sp<sup>2</sup> Fraction. *Phys. Rev. B: Condens. Matter Mater. Phys.* **2012**, *86*, 235423.
- (13) Samadi Khoshkhoo, M.; Maiti, S.; Schreiber, F.; Chassé, T.; Scheele, M. Surface Functionalization with Copper Tetraaminophthalocyanine Enables Efficient Charge Transport in Indium Tin Oxide Nanocrystal Thin Films. *ACS Appl. Mater. Interfaces* **2017**, *9*, 14197–14206.
- (14) Sun, S.; Li, P.; Liang, S.; Yang, Z. Diversified Copper Sulfide (Cu<sub>2-x</sub>S) Micro-/Nanostructures: A Comprehensive Review on Synthesis, Modifications and Applications. *Nanoscale* **2017**, *9*, 11357–11404.
- (15) Van Der Stam, W.; Gudjonsdottir, S.; Evers, W. H.; Houtepen, A. J. Switching between Plasmonic and Fluorescent Copper Sulfide Nanocrystals. *J. Am. Chem. Soc.* **2017**, *139*, 13208–13217.
- (16) Vinokurov, K.; Elimelech, O.; Millo, O.; Banin, U. Copper Sulfide Nanocrystal Level Structure and Electrochemical Functionality towards Sensing Applications. *ChemPhysChem* **2016**, *17*, 675–680.
- (17) Brewer, A. S.; Arnold, M. S. Field-Effect Measurements of Mobility and Carrier Concentration of Cu<sub>2</sub>S Colloidal Quantum Dot Thin Films after Ligand Exchange. *Thin Solid Films* **2014**, *567*, 91–95.
- (18) Otelaja, O. O.; Ha, D. H.; Ly, T.; Zhang, H.; Robinson, R. D. Highly Conductive Cu<sub>2-x</sub>S Nanoparticle Films through Room-Temperature Processing and an Order of Magnitude Enhancement of Conductivity via Electrophoretic Deposition. *ACS Appl. Mater. Interfaces* **2014**, *6*, 18911–18920.
- (19) Bekenstein, Y.; Elimelech, O.; Vinokurov, K.; Millo, O.; Banin, U. Charge Transport in Cu<sub>2</sub>S Nanocrystals Arrays: Effects of Crystallite Size and Ligand Length. *Z. Phys. Chem.* **2015**, *229*, 179–190.
- (20) Aigner, W.; Nenova, G. K.; Sliem, M. A.; Fischer, R. A.; Stutzmann, M.; Pereira, R. N. Electronic Changes Induced by Surface Modification of Cu<sub>2-x</sub>S Nanocrystals. *J. Phys. Chem. C* **2015**, *119*, 16276–16285.
- (21) Bekenstein, Y.; Vinokurov, K.; Keren-Zur, S.; Hadar, I.; Schilt, Y.; Raviv, U.; Millo, O.; Banin, U. Thermal Doping by Vacancy Formation in Copper Sulfide Nanocrystal Arrays. *Nano Lett.* **2014**, *14*, 1349–1353.
- (22) Scheele, M.; Brütting, W.; Schreiber, F. Coupled Organic–inorganic Nanostructures (COIN). *Phys. Chem. Chem. Phys.* **2015**, *17*, 97–111.
- (23) Xie, Y.; Riedinger, A.; Prato, M.; Casu, A.; Genovese, A.; Guardia, P.; Sottini, S.; Sangregorio, C.; Miszta, K.; Ghosh, S.; Pellegrino, T.; Manna, L. Copper Sulfide Nanocrystals with Tunable Composition by Reduction of Covellite Nanocrystals with Cu<sup>+</sup> Ions. *J. Am. Chem. Soc.* **2013**, *135*, 17630–17637.
- (24) Jung, S. H.; Choi, J. H.; Yang, S. M.; Cho, W. J.; Ha, C. S. Syntheses and Characterization of Soluble Phthalocyanine Derivatives for Organic Electroluminescent Devices. *Mater. Sci. Eng., B* **2001**, *85*, 160–164.
- (25) Sharma, R.; Sawvel, A. M.; Barton, B.; Dong, A.; Buonsanti, R.; Llordes, A.; Schaible, E.; Axnanda, S.; Liu, Z.; Urban, J. J.; Nordlund, N. D.; Kisielowski, C.; Milliron, D. J. Nanocrystal Superlattice Embedded within an Inorganic Semiconducting Matrix by In Situ

Ligand Exchange: Fabrication and Morphology. *Chem. Mater.* **2015**, *27*, 2755–2758.

(26) Dong, A.; Chen, J.; Oh, S. J.; Koh, W. K.; Xiu, F.; Ye, X.; Ko, D. K.; Wang, K. L.; Kagan, C. R.; Murray, C. B. Multiscale Periodic Assembly of Striped Nanocrystal Superlattice Films on a Liquid Surface. *Nano Lett.* **2011**, *11*, 841–846.

(27) Maiti, S.; André, A.; Banerjee, R.; Hagenlocher, J.; Konovalov, O.; Schreiber, F.; Scheele, M. Monitoring Self-Assembly and Ligand Exchange of PbS Nanocrystal Superlattices at the Liquid/Air Interface in Real Time. *J. Phys. Chem. Lett.* **2018**, *9*, 739–744.

(28) Joseph, Y.; Guse, B.; Vossmeier, T.; Yasuda, A. Gold Nanoparticle/Organic Networks as Chemiresistor Coatings: The Effect of Film Morphology on Vapor Sensitivity. *J. Phys. Chem. C* **2008**, *112*, 12507–12514.

(29) Luther, J. M.; Jain, P. K.; Ewers, T.; Alivisatos, A. P. Localized Surface Plasmon Resonances Arising from Free Carriers in Doped Quantum Dots. *Nat. Mater.* **2011**, *10*, 361–366.

(30) Dorfs, D.; Härtling, T.; Miszta, K.; Bigall, N. C.; Kim, M. R.; Genovese, A.; Falqui, A.; Povia, M.; Manna, L. Reversible Tunability of the Near-Infrared Valence Band Plasmon Resonance in  $\text{Cu}_{2-x}\text{Se}$  Nanocrystals. *J. Am. Chem. Soc.* **2011**, *133*, 11175–11180.

(31) Wolf, A.; Kodanek, T.; Dorfs, D. Tuning the LSPR in Copper Chalcogenide Nanoparticles by Cation Intercalation, Cation Exchange and Metal Growth. *Nanoscale* **2015**, *7*, 19519–19527.

(32) Kumar, P.; Nagarajan, R. An Elegant Room Temperature Procedure for the Precise Control of Composition in the Cu-S System. *Inorg. Chem.* **2011**, *50*, 9204–9206.

(33) Gu, F.; Xu, G. Q.; Ang, S. G. Fabrication of CuTAPc Polymer Nanowires and Nanotubes by Electropolymerization. *Nanotechnology* **2008**, *19*, 145606.

(34) Surovtsev, N. V.; Adichtchev, S. V.; Duda, T. A.; Pokrovsky, L. D.; Sveshnikova, L. L. New Surface-Enhanced Raman Scattering Active Substrate Fabricated by Use of the Langmuir-Blodgett Technique. *J. Phys. Chem. C* **2010**, *114*, 4803–4807.

(35) Renaud, G.; Lazzari, R.; Leroy, F. Probing Surface and Interface Morphology with Grazing Incidence Small Angle X-Ray Scattering. *Surf. Sci. Rep.* **2009**, *64*, 255–380.

(36) Maiti, S.; Sanyal, M. K.; Jana, M. K.; Runge, B.; Murphy, B. M.; Biswas, K.; Rao, C. N. R. Evidence of Contact Epitaxy in the Self-Assembly of HgSe Nanocrystals Formed at a Liquid-Liquid Interface. *J. Phys.: Condens. Matter* **2017**, *29*, 09S101.

(37) Ren, B.; Wang, L.; Huang, J.; Tang, K.; Yang, Y.; Wang, L. Metal-Semiconductor Transition in  $\text{CuS-Cu}_{1.8}\text{S}$  Mixed Phase Thin Films. *Vacuum* **2015**, *112*, 70–72.

(38) Liu, H.; Pourret, A.; Guyot-Sionnest, P. Mott and Efros-Shklovskii Variable Range Hopping in CdSe Quantum Dots Films. *ACS Nano* **2010**, *4*, 5211–5216.

(39) Gainov, R. R.; Dooglav, A. V.; Pen'kov, I. N.; Mukhamedshin, I. R.; Mozgova, N. N.; Evlampiev, I. A.; Bryzgalov, I. A. Phase Transition and Anomalous Electronic Behavior in the Layered Superconductor CuS Probed by NQR. *Phys. Rev. B: Condens. Matter Mater. Phys.* **2009**, *79*, 075115.

(40) Jain, P. K.; Huang, W.; El-Sayed, M. A. On the Universal Scaling Behavior of the Distance Decay of Plasmon Coupling in Metal Nanoparticle Pairs: A Plasmon Ruler Equation. *Nano Lett.* **2007**, *7*, 2080–2088.

(41) Wei, H.; Grundmann, M.; Lorenz, M. Confinement-Driven Metal-Insulator Transition and Polarity-Controlled Conductivity of Epitaxial  $\text{LaNiO}_3/\text{LaAlO}_3(111)$  Superlattices. *Appl. Phys. Lett.* **2016**, *109*, 082108.

(42) Joseph, Y.; Guse, B.; Yasuda, A.; Vossmeier, T. Chemiresistor Coatings from Pt- and Au-Nanoparticle/Nonanedithiol Films: Sensitivity to Gases and Solvent Vapors. *Sens. Actuators, B* **2004**, *98*, 188–195.

(43) Olichwer, N.; Meyer, A.; Yesilmen, M.; Vossmeier, T. Gold Nanoparticle Superlattices: Correlating Chemiresistive Responses with Analyte Sorption and Swelling. *J. Mater. Chem. C* **2016**, *4*, 8214–8225.

(44) Belghachi, A.; Collins, R. A. Humidity Response of Phthalocyanine Gas Sensors. *J. Phys. D: Appl. Phys.* **1988**, *21*, 1647–1651.

(45) Hassinen, A.; Moreels, I.; De Nolf, K.; Smet, P. F.; Martins, J. C.; Hens, Z. Short-Chain Alcohols Strip X-Type Ligands and Quench the Luminescence of PbSe and CdSe Quantum Dots, Acetonitrile Does Not. *J. Am. Chem. Soc.* **2012**, *134*, 20705–20712.

(46) García-Berrios, E.; Gao, T.; Woodka, M. D.; Maldonado, S.; Brunschwig, B. S.; Ellsworth, M. W.; Lewis, N. S. Response versus Chain Length of Alkanethiol-Capped Au Nanoparticle Chemiresistive Chemical Vapor Sensors. *J. Phys. Chem. C* **2010**, *114*, 21914–21920.

(47) Fu, K.; Li, S.; Jiang, X.; Wang, Y.; Willis, B. G. DNA Gold Nanoparticle Nanocomposite Films for Chemiresistive Vapor Sensing. *Langmuir* **2013**, *29*, 14335–14343.

(48) Hubble, L. J.; Cooper, J. S.; Sosa-Pintos, A.; Kiiveri, H.; Chow, E.; Webster, M. S.; Wiczorek, L.; Raguse, B. High-Throughput Fabrication and Screening Improves Gold Nanoparticle Chemiresistor Sensor Performance. *ACS Comb. Sci.* **2015**, *17*, 120–129.

(49) Rigoni, F.; Drera, G.; Pagliara, S.; Perghem, E.; Pintossi, C.; Goldoni, A.; Sangaletti, L. Gas Sensing at the Nanoscale: Engineering SWCNT-ITO Nano-Heterojunctions for the Selective Detection of  $\text{NH}_3$  and  $\text{NO}_2$  target Molecules. *Nanotechnology* **2017**, *28*, 035502.

(50) Samadi Khoshkhou, M.; Joseph, Y.; Maiti, S.; Schreiber, F.; Chassé, T.; Scheele, M. Tunable Charge Transport in Hybrid Superlattices of Indium Tin Oxide Nanocrystals and Metal Phthalocyanines—Toward Sensing Applications. *Adv. Mater. Interfaces* **2018**, *5*, 1701623.

(51) Lupan, O.; Postica, V.; Gröttrup, J.; Mishra, A. K.; De Leeuw, N. H.; Carreira, J. F. C.; Rodrigues, J.; Ben Sedrine, N.; Correia, M. R.; Monteiro, T.; Cretu, H. V.; Tiginyanu, I.; Smazna, D.; Mishra, Y. K.; Adelung, R. Hybridization of Zinc Oxide Tetrapods for Selective Gas Sensing Applications. *ACS Appl. Mater. Interfaces* **2017**, *9*, 4084–4099.

(52) Dovgolevsky, E.; Konvalina, G.; Tisch, U.; Haick, H. Monolayer-Capped Cubic Platinum Nanoparticles for Sensing Nonpolar Analytes in Highly Humid Atmospheres. *J. Phys. Chem. C* **2010**, *114*, 14042–14049.

(53) Wang, X. J.; Wang, W.; Liu, Y. L. Enhanced Acetone Sensing Performance of Au Nanoparticles Functionalized Flower-like ZnO. *Sens. Actuators, B* **2012**, *168*, 39–45.